mater.scichina.com link.springer.com

Published online 24 September 2021 | https://doi.org/10.1007/s40843-021-1775-2
Sci China Mater 2022, 65(3): 653–662

Self-catalyzed growth of Zn/Co-N-C carbon nanotubes derived from metal-organic frameworks as efficient oxygen reduction catalysts for Zn-air battery

Jing Zhang, Ye Chen, Yang Liu, Xupo Liu* and Shuyan Gao*

ABSTRACT **Designing cost-effective and high-performance carbon-based oxygen reduction reaction (ORR) electrocatalysts is crucial in the development of Zn-air batteries (ZABs). In this study, a facile one-pot synthesis approach is engineered to construct Zn/Co-N-C carbonaceous polyhedrons interconnected with self-catalyzed-grown carbon nanotubes (CNTs) from zeolitic imidazolium frameworks linked with graphene oxide nanosheets. The special N-doped three-dimensional (3D) carbon matrix allows manipulating the exposure of active sites and the synergistic interaction between metal nanoparticles and CNTs. The as-synthesized catalyst features impressive ORR activity in 0.1 mol L^{-1} KOH ($E_{1/2}$ = 0.83 V) and 0.5 mol L^{-1} H_2SO_4 ($E_{1/2}$ = 0.73 V), satisfactory cycling stability and methanol resistance comparable to those of the benchmark Pt/C catalyst ($E_{1/2}$ = 0.80 V in 0.1 mol L^{-1} KOH, $E_{1/2}$ = 0.75 V in 0.5 mol L^{-1} H_2SO_4). Furthermore, the as-established ZAB demonstrates a competitive peak power density (90 mW cm^{-2}) and prominent long-term stability, which are better than those of devices based on the commercial Pt/C catalyst (82 mW cm^{-2}). This work provides promising guidance for fabricating highly effective ORR catalysts with *in situ* formed CNTs, which can be applied in portable ZAB-related devices.**

Keywords: oxygen reduction reaction, carbon nanotubes, self-catalyzed growth, synergistic interaction, Zn-air batteries

INTRODUCTION

The heavy dependence of contemporary society on fossil fuels generates alarming global pollution and arouses serious concerns about the energy crisis [1–3]. Tremendous endeavors have been dedicated to exploring next-generation renewable and clean energy storage technology [4]. Zn-air batteries (ZABs) are excellent alternatives to satisfy the requirement of flexible energy-storage devices because of their high theoretical energy density (1086 W h kg^{-1}), reliable safety, and environmental benignity [5,6]. In general, platinum (Pt)-based electrocatalysts have been extensively utilized to enhance the sluggish oxygen reduction reaction (ORR) that occurs at the air electrode of ZABs. Nevertheless, the scarcity, prohibitive cost, and weak durability of Pt-based materials have impeded the long-term commercial development of ZABs [7,8]. Hence, research communities have devoted tremendous efforts to exploring highly effective non-Pt-based materials, such as metal chalcogenides, metal oxides, metal carbonitrides, and metal-nitrogen-carbon (M-N-C) [9,10]. To date, M-N-C materials (M = Fe, Co, Ni, Mn, etc.) are commonly employed as cathode materials to substitute platinum-based materials because of their outstanding ORR performance, flexibility with dopants, long-term stability, and encouraging electrical conductivity [11].

Recently, metal-organic frameworks (MOFs), constructed by organic ligands and transition metal cores, are favorable platforms for fabricating high-performance ORR catalysts because of their well-designed porous structure, flexible composition, and high surface area [12–16]. Among numerous MOFs, zeolitic imidazole frameworks (ZIFs) have attracted enormous attention as precursors for developing M-N-C catalysts [17–20]. The intrinsic electronic structure and extrinsic properties (such as pore structure and size, degree of graphitization) of materials are crucial aspects for promoting ORR activity [21]. Volcano plots implemented in intensive studies have indicated that the incorporation of metal/heteroatom doping can regulate the local electronic structure of catalysts through adopting the spin density, charge effect, and ligand effect. As for non-noble metal ORR electrocatalysts, functional species, including heteroatom dopants, targeted M-N-C sites, and appropriate defects, are active moieties. These capable active sites can stimulate the following oxygen–oxygen bond breakage toward a desirable 4-electron pathway, resulting in excellent activity and durability. Previous studies suggested that the degree of graphitization is another significant factor affecting ORR performance because the ORR is an electron transfer process [22]. The graphitization degree can be manipulated through heteroatom doping, hierarchical porosity, and functional moieties [23,24]. Although several ZIF-derived nanocarbon materials doped with heteroatoms and transition metals have been investigated as ORR electrocatalysts, their electrochemical activity still needs to be accelerated to satisfy practical applications.

Nitrogen-doped carbon nanotubes (N-CNTs) are widely utilized as excellent catalysts for accelerating mass and electron transfer in ORR [25,26]. Density functional theory (DFT) simulations have shown that the density of state around the Fermi level could be increased because of the synergetic interaction between the graphitic-N and encapsulated metal nanoparticles in N-CNTs, thus reducing the work function and further yielding improved ORR activity. Moreover, academic and industrial investigations have confirmed that the introduc-

School of Materials Science and Engineering, Henan Normal University, Xinxiang 453007, China
* Corresponding authors (emails: liuxupo@htu.edu.cn (Liu X); shuyangao@htu.cn (Gao S))

tion of electron-drawing oxygen atoms into the conjugated nanotubes provides additional sites for generating positive charges on the surrounding carbon atoms, energetically facilitating the OH* desorption in ORR [27,28]. Hence, N-CNTs derived from MOFs *via* the bottom-up strategy have intrigued extensive attention for ORR application in recent years [29–31]. In addition, graphene can be employed as either host materials or active ingredients to improve ORR performance [32–35]. On the one hand, graphene oxide (GO) with a large specific surface area and good electrical conductivity is adopted as the conductive carbon support. On the other hand, the catalytic performance of graphene-based composite catalysts can be improved through the synergistic effect between graphene and ZIF-8-derived N-doped carbon materials. In conclusion, the interaction between MOF-derived carbon and graphene decreases the electron-transfer resistance and provides additional catalytic active sites for the prepared catalysts. Therefore, the three-dimensional (3D) carbonaceous polyhedrons interconnected with N-CNTs derived from MOFs and graphene are profitable for achieving efficient ORR catalysts. However, previous studies rarely reported this topic.

In this study, a facile one-pot synthesis is engineered to construct ZIF-derived graphene-based self-catalyzed Zn/Co-N-C polyhedrons interconnected by CNTs. Highly graphitized porous frameworks are formed by the introduction of moderate GO, which can afford robust frameworks with rich pores and accelerate the transport of O_2 and electrolytes. During carbonization, the carbon materials formed by the decomposition of imidazole are supposed to reduce the adsorbed Co ions to produce metal nanoparticles. With the neighboring solid carbon as ingredients, the nanoparticles on the surface can catalyze the growth of N-CNTs, and then the metal nanoparticles are simultaneously encapsulated in the N-CNTs. The resulting N-CNTs can reduce the aggregation of carbonaceous polyhedrons because of the strong π-π stacking interaction, thus increasing the number of accessible active sites and boosting the electrochemical activity. As expected, the optimized ZnCo-NGC exhibits impressive ORR performances in 0.1 mol L^{-1} KOH ($E_{1/2}$ = 0.83 V *vs*. reversible hydrogen electrode (RHE)) and 0.5 mol L^{-1} H_2SO_4 solution ($E_{1/2}$ = 0.73 V), comparable to those of the benchmark Pt/C catalyst ($E_{1/2}$ = 0.80 V in 0.1 mol L^{-1} KOH; $E_{1/2}$ = 0.75 V in 0.5 mol L^{-1} H_2SO_4). In addition, ZnCo-NGC catalysts display excellent long-term durability and methanol resistance in alkaline and acidic electrolytes. Importantly, the homemade ZAB delivers the prominent property of a max power density of 90 mW cm^{-2} and impressive cycling durability, surpassing those of devices assembled with Pt/C catalysts. This work may provide a profound pathway for designing advanced metal-air cathode catalysts.

EXPERIMENTAL SECTION

Materials

2-Methylimidazole (2-MEIM, $C_4H_6N_2$, 98%), cobalt(III) acetylacetonate ($Co(acac)_3$, $C_{15}H_{21}CoO_6$, 98%), potassium hydroxide (KOH, 90%), and zinc acetate ($Zn(OAc)_2$, analytical reagent (AR)) were purchased from Aladdin Industrial Corporation (Shanghai, China). GO powders were obtained from Suzhou Carbon Technology Co., Ltd. Zinc nitrate hexahydrate ($Zn(NO_3)_2{\cdot}6H_2O$, AR) was acquired from Tianjin Kermel Chemical Reagent Co., Ltd. Methanol (CH_3OH, AR) was provided by Tianjin Deen Chemical Reagent Co., Ltd. Sulfuric acid (H_2SO_4, AR) and hydrochloric acid (HCl, AR) were purchased from Yantai Shuangshuang Chemical Co., Ltd. Nafion solution (5%) and 20 wt% Pt/C were obtained from Johnson Matthey Company and DuPont Company, respectively. Deionized (DI) water with a specific resistance (18.25 MΩ) was employed. The raw materials were used directly without further purification.

Preparation of ZIF-8, GO@ZIF-8, Co@ZIF-8, and Co&GO@ZIF-8 precursors

2-MEIM (6.5 g) was mixed with methanol (100 mL) under ultrasonic treatment for approximately 10 min to gain solution A. $Zn(NO_3)_2{\cdot}6H_2O$ (3 g) was dissolved into methanol (50 mL) by ultrasonication to acquire solution B. Then, solution B was subsequently poured into solution A, followed by continuous stirring at room temperature for 24 h. The obtained precipitates were centrifuged, washed several times with methanol, and then dried under vacuum at 60°C overnight. The achieved products were ZIF-8 precursors.

The preparation of GO@ZIF-8, Co@ZIF-8, and Co&GO@ZIF-8 precursors was similar to that of ZIF-8 except the diverse solutions B. For GO@ZIF-8, solution B was composed of $Zn(NO_3)_2{\cdot}6H_2O$ (3 g) and GO (0.2 g). For Co@ZIF-8, solution B consisted of $Zn(NO_3)_2{\cdot}6H_2O$ (3 g) and cobalt(III) acetylacetonate (0.514 g). For Co&GO@ZIF-8, solution B was obtained using $Zn(NO_3)_2{\cdot}6H_2O$ (3 g), cobalt(III) acetylacetonate (0.514 g), and GO (0.2 g). The other synthesis conditions were similar to those used in the preparation of ZIF-8.

Preparation of Zn-NC, Zn-NGC, ZnCo-NC, and ZnCo-NGC

The as-prepared precursors were placed into a tube furnace and heated at 900°C for 3 h under flowing nitrogen gas (ramp rate ~5°C min^{-1}). After being cooled down to room temperature, the collected black powders were soaked in 2 mol L^{-1} HCl, washed with DI water, and then dried at 60°C. The products derived from ZIF-8, GO@ZIF-8, Co@ZIF-8, and Co&GO@ZIF-8 precursors were denoted as Zn-NC, Zn-NGC, ZnCo-NC, and ZnCo-NGC, respectively.

Physical characterization

The micromorphology of the samples was obtained through scanning electron microscopy (SEM, Zeiss Supra 40) and transmission electron microscopy (TEM, JEOL JEM-2100). The crystal structure was determined using powder X-ray diffraction (XRD) on a Bruker D8 diffractometer with Cu-Kα radiation (λ = 0.154 nm). The specific surface areas and the corresponding pore size distributions were calculated at 77 K on a Quantachrome Autosorb Station (iQ2) instrument by using the Brunauer-Emmett-Teller (BET) and non-local DFT (NL-DFT) methods, respectively. Raman spectra were obtained on a Renishaw spectrometer with 532 nm excitation. The chemical compositions of the samples were analyzed by X-ray photoelectron spectroscopy (XPS) on an ESCALAB250 spectrometer with the Al Kα X-ray as the excitation source. The hydrophilicity of the samples was measured using a contact angle meter (KRüSS DSA25).

Electrochemical characterization

Electrochemical tests were recorded by using a three-electrode cell on a CHI6043E workstation (Chenhua, Shanghai, China). The three-electrode system was assembled using commercial

glassy carbon (GC, diameter = 3/4/5 mm) as the working electrode, Hg/HgO/KOH (1.0 mol L^{-1}) or saturated calomel electrode (saturated KCl) as the reference electrode, and Pt foil (1 cm^2) as the reference electrode. The N_2 or O_2-saturated 0.1 mol L^{-1} KOH or 0.5 mol L^{-1} H_2SO_4 electrolyte was adopted as the electrolyte. To fabricate the catalyst ink, 1 mg of catalysts was added in 0.12 mL of solution, including 0.02 mL of 5% Nafion and 0.10 mL of DI water with ultrasound to obtain a uniform ink. Afterward, 5/10/12 μL of catalyst ink was dropped on a 3/4/5-mm clean GC electrode and then dried naturally. For comparison, a commercial Pt/C catalyst was prepared using the same process. O_2 or N_2 flow was introduced into the media for a period of time before the measurement to reach the saturation state. Cyclic voltammetry (CV) curves were measured on the working electrode-coated as-prepared catalysts in alkaline or acidic electrolyte at a scan rate of 10 mV s^{-1} from 0 to 1.2 V (*vs.* RHE).

Rotating disk electrode tests were gauged in O_2-saturated electrolytes ranging from 400 to 2025 r min^{-1} at a scan rate of 10 mV s^{-1}. The electron transfer number (n) was calculated from the Koutecky-Levich (K-L) equation as follows:

$$\frac{1}{J} = \frac{1}{J_L} + \frac{1}{J_k} = \frac{1}{B\omega^{1/2}} + \frac{1}{J_k}, \quad (1)$$

where J, J_L, and J_k represent the measured current density, the diffusion-limiting density and kinetic current density, respectively. The ω stands for the electrode rotation rate. B can be achieved from the following equation: $B = 0.2nFC_0D^{2/3}\nu^{-1/6}$, where F is the Faraday constant (96,485 C mol^{-1}), C_0 refers to the bulk O_2 concentration (1.2×10^{-3} mol cm^{-3}), D is the diffusion coefficient of O_2 in 0.1 mol L^{-1} KOH electrolyte (1.9×10^{-5} cm^2 s^{-1}), and ν is the kinematic viscosity of the electrolyte (0.01 cm^2 s^{-1}).

Rotating ring-disk electrode (RRDE) measurements were employed at a constant rotation speed of 1600 r min^{-1} and a scan rate of 10 mV s^{-1}. The electron transfer number (n) and peroxide yield (H_2O_2%) were obtained by the following equations:

$$H_2O_2\% = 200i_r / (i_d \times N + i_r), \quad (2)$$

$$n = 4i_d / (i_d + i_r / N), \quad (3)$$

where i_r, i_d represent the ring current and the disk current, respectively. N is the collection efficiency of the Pt ring (N = 0.37).

As for the methanol tolerance test, CV curves from 0 to 1.2 V were measured in oxygen-saturated alkaline or acidic solution at the scan rate of 10 mV s^{-1}, followed by the injection of 3 mL of 3 mol L^{-1} methanol. Electrochemical stability tests were performed in O_2-saturated electrolyte after continuous CV measurement of 6000 or 3000 cycles at 0–1.2 V (scan rate ~50 mV s^{-1}). The scanning time per 1000 cycles was 34,000 s. Electrochemical impedance spectroscopy (EIS) was conducted ranging from 100 kHz to 1 Hz with a voltage amplitude of 5 mV. All quoted potentials were corrected to the RHE.

ZAB testing

The performance of ZABs was carried out using home-built electrochemical cells. Zn foil was applied as the anode, and the electrolyte was 6 mol L^{-1} KOH aqueous solution filled with 0.2 mol L^{-1} $Zn(OAc)_2$. Typically, 5 mg of ZnCo-NGC was dispersed into a homogeneous catalyst ink, including 50 μL of 5% Nafion solution, 500 μL of ethanol, and 25 μL of polytetrafluoroethylene aqueous suspension (5 wt%). Then, the acquired ink was dripped on the surface of carbon paper, guaranteeing a catalyst loading of 2 mg cm^{-2}. For comparison, the air electrode was also produced by the deposition of Pt/C catalysts. All data were measured through the as-established cell using a CHI660E system at room temperature.

RESULTS AND DISCUSSION

Physical properties and composition analysis

As shown in Scheme 1, a facile ZIF-directed strategy is engineered to construct the 3D carbonaceous polyhedrons linked by CNTs through pyrolyzing Co ions encapsulated in ZIF-8 intercalating GO sheets. GO containing epoxy and hydroxyl functional groups on both sides is utilized to chelate with metal ions in ZIFs. On the basis of the intercalation between GO and metal ions, GO can coordinate with the Zn ions in ZIF-8 and partially substitute 2-MEIM ligands while maintaining the underlying coordination frameworks of ZIF-8. At the same time, the Co guest ions are *in situ* encapsulated in the ZIF-8 cages that are achieved by the assembly of Zn^{2+} and 2-MEIM in methanol. Then, the formed Co&GO@ZIF-8 precursors are transformed into N-doped carbon nano-polyhedrons through high-temperature pyrolysis. During pyrolysis, such hybrid coordination facilitates Zn evaporation and Co-N formation at the same time. Interestingly, during the pyrolysis at 900°C under N_2 atmosphere, ZIF-8 and GO are transformed into nitrogen-doped porous carbon. Meanwhile, $Co(acac)_3$ within the cages is reduced by the carbonization of organic linkers, leading to the formation of Co clusters/nanoparticles on the surface of poly-

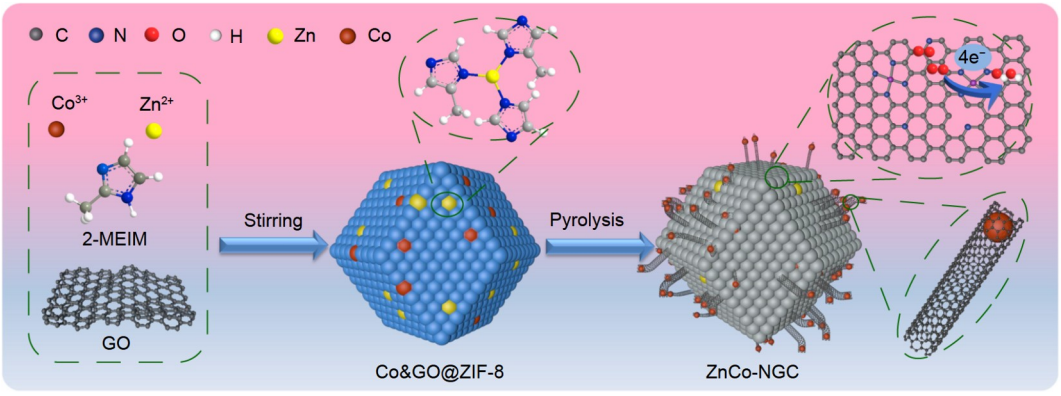

Scheme 1 Schematic of synthesizing the ZnCo-NGC catalysts.

hedrons. These surface clusters/nanoparticles possess strong catalytic activity toward the spontaneous growth of CNTs derived from the nitrogenous organic linkers of ZIF-8. Accordingly, the continuous diffusion of carbon atoms reaches the surface of Co nanoparticles, which are gradually enclosed into the growing CNTs. Accompanying with the constant diffusion of carbon atoms, the CNTs continue to elongate until the solid carbon matrix is exhausted [36]. The *in situ* formed CNTs can not only heighten the conductivity of catalysts, but also deliver abundant transport channels. Moreover, the special N-CNT architecture can effectively reduce the aggregation of carbonaceous polyhedrons, leading to additional exposed active sites and thus boosting the electrochemical activity.

SEM and TEM characterizations were conducted to illustrate the structure of the samples, and the corresponding results are depicted in Fig. 1. The Co&GO@ZIF-8 with initial polyhedral ZIF-8 structure can be observed from the SEM images (Fig. 1a, b). After pyrolysis, the surface of ZnCo-NGC becomes much rougher, and some CNTs grow from the surfaces of the cubes (Fig. 1c–e), which can be further demonstrated by TEM images (Fig. S1a–c). ZnCo-NGC catalysts possess CNTs and enclosed metal particles. During the thermal treatment, the organic ligands in ZIF-8 are broken up into reductive gas (e.g., NH_3/H_2) to reduce Co ions into nanoparticles. Meanwhile, the organic residuals decompose to generate carbon radicals, which are eventually converted into CNTs through the self-catalyzed effect. For ZnCo-NGC, the homogeneous dispersion of N, O, Co, and Zn on the entire carbon structure is detected by the elemental mapping (Fig. 1f). The TEM image (Fig. 1g) also confirms that the Co nanoparticles are encapsulated in the 3D interconnected heterostructure of N-CNTs. The high-resolution TEM (HRTEM) image (Fig. 1h) exhibits a clear-defined lattice fringe of 0.201 nm, which matches with metallic Co (111). Fig. 1i indicates the (002) plane of the graphitic structure of ZnCo-NGC, which is beneficial for enhancing the conductivity of catalysts. The possible formation of the unique polyhedral structure interconnected with CNTs is illustrated in Fig. 1j. During the heat treatment, the Co species firstly segregated from the polyhedron intermediates precipitate on the surface of polyhedrons to produce Co nanoparticles. Then, the continuous diffusion of carbon atoms reaches the surface of Co nanoparticles, and the high self-catalyzed effect of Co nanoparticles is profitable for the *in situ* growth of CNTs. After pyrolysis, the Co nanoparticles are enclosed in the well-grown CNTs. In short, the self-catalyzed approach accelerates the continuous growth of CNTs, which can establish fast electron conductivity and prevent

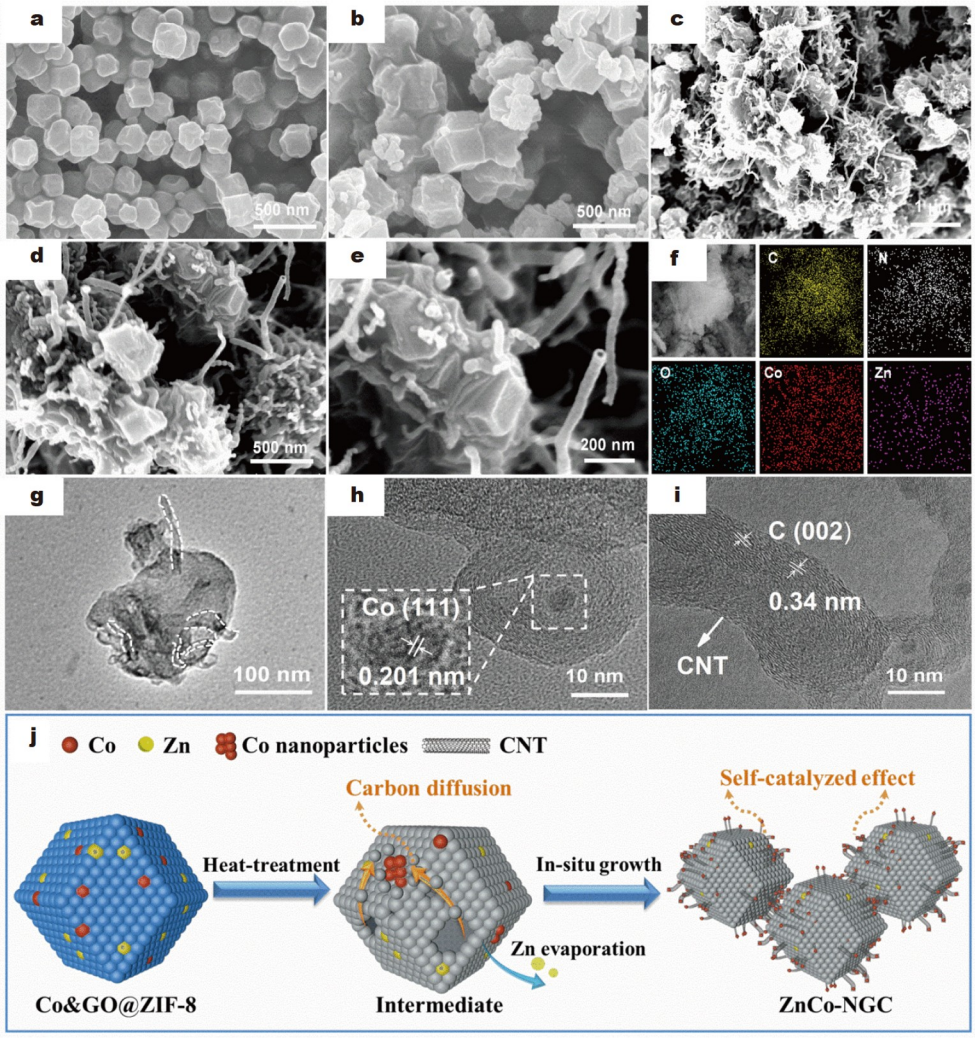

Figure 1 SEM images of (a) ZIF-8, (b) Co&GO@ZIF-8, and (c–e) ZnCo-NGC. (f) The corresponding elemental mapping images of ZnCo-NGC. (g–i) TEM (HR-TEM) images of ZnCo-NGC. (j) Schematic of the self-catalyzed growth of ZnCo-NGC.

the aggregation of carbon nano-polyhedra.

The crystal structure of the obtained catalysts can be detected using XRD. The diffraction peaks of all precursors are consistent with ZIF-8 (Fig. S2). After pyrolysis and soaking with HCl, two broad peaks at 23°–26° and 43° appear obviously for Zn-NC and Zn-NGC, which correspond to the (002) and (100) lattice planes of graphitic carbon. As for ZnCo-NC and ZnCo-NGC, a strong peak at 23°–26° is observed, which corresponds to the (002) plane of graphitic carbon, and the peak located at 44.3° can be attributed to (111) of the metallic Co (Fig. 2a). Nitrogen sorption measurements are conducted to investigate the porous structure of the prepared catalysts (Fig. 2b, c). The combined hybrid type-I and IV isotherms with an H3 hysteresis loop indicate the coexistence of micropores and mesopores for ZnCo-NGC. Obtained using the BET and NL-DFT methods, all pore texture parameters of Zn-NC, Zn-NGC, ZnCo-NC, and ZnCo-NGC are presented in Table S1. Notably, ZnCo-NGC possesses the largest micropore surface area of 263.3 $m^2 g^{-1}$, which is believed to expose more accessible active sites and favor the entrance and release of oxygen molecules [37]. This porous microstructure is mostly contributed by the evaporation of Zn species and the self-catalyzed generation of CNTs. The hierarchical porous carbon structure and interconnected CNTs allow the convenient storage and transmission of electrolyte ions during ORR. In addition, the production of graphitic C is confirmed by Raman tests (Fig. 2d). The D band at 1336 cm^{-1} stems from the edge defects, and the G band at 1583 cm^{-1} corresponds to the sp^2-bonded graphitic carbon. The lower intensity ratio of D and G bands (I_D/I_G) for ZnCo-NGC (I_D/I_G = 1.12) suggests the presence of more sp^2-hybridized graphitic carbon atoms compared with Zn-NC (I_D/I_G = 1.30), Zn-NGC (I_D/I_G = 1.24) and ZnCo-NC (I_D/I_G = 1.14). Graphitic carbon helps facilitate the charge transfer rate and stabilize the structure of polyhedron interconnected CNTs [31,38]. The surface wettability of ZnCo-NGC was measured to be 5.8° by the water contact angle test (Fig. S3). Such good hydrophilic ability is attributed to the existence of hydrophilic functional groups in ZnCo-NGC, which can facilitate valid ion transfer and consequently enhance catalytic performance [39].

The chemical states and compositions of the catalysts were further investigated using XPS. The XPS survey spectrum of ZnCo-NGC indicates the existence of Zn, Co, C, N, and O (Fig. S4). Zn species in ZnCo-NGC have not completely volatilized and have been transformed to Zn-N groups maintained in the catalyst, which would be beneficial for supporting the stability of the frameworks (Fig. S5). The C 1s high-resolution spectrum (Fig. 2e) is divided into four peaks, which are associated with carbon atom bonds: C-sp^2 (284.6 eV), C-sp^3 (285.5 eV), C–N (286.9 eV), and C=O/C=N (288.9 eV). In the case of N-species, four types of N-containing groups for Zn-NC and Zn-NGC have been verified, including pyridinic (398.5 eV), pyrrolic (400.2 eV), graphitic (401.1 eV), and oxidized (404.3 eV) nitrogen species [40]. The N 1s spectra of ZnCo-NC and ZnCo-NGC can be well-fitted to four peaks located at 398.5, 399.6, 400.2, and 401.2 eV, which correspond to pyridinic-N, Zn/Co-N_x, pyrrolic-N, and graphitic-N, respectively (Fig. 2f). The contents of different N types are regulated by introducing

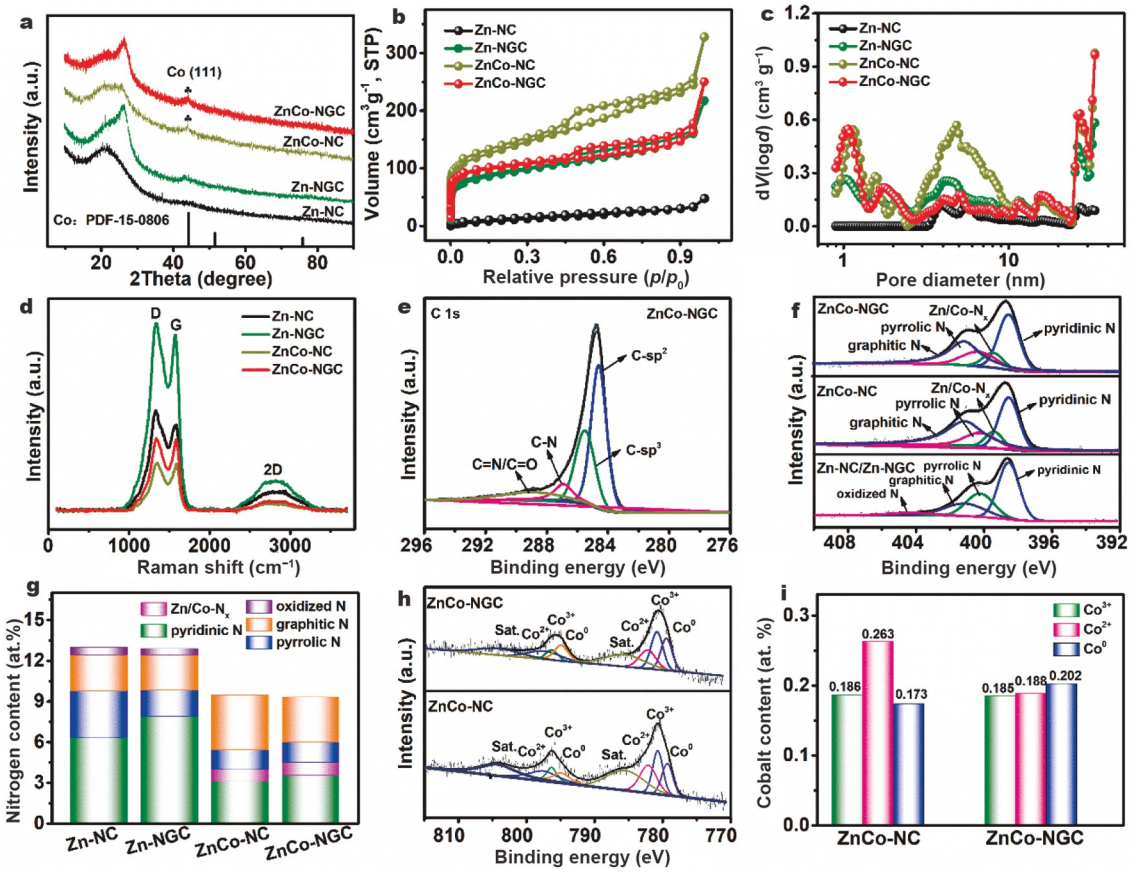

Figure 2 (a) XRD patterns. (b) N_2 adsorption-desorption isotherms. (c) Mesopore size distribution by the DFT method. (d) Raman spectra. (e) C 1s XPS spectra. (f) N 1s XPS spectra. (g) N contents and chemical forms. (h) Co 2p XPS spectra. (i) Co contents and chemical forms of ZnCo-NC and ZnCo-NGC.

GO or cobalt(III) acetylacetonate. By comparison with ZnCo-NC, ZnCo-NGC catalyst possesses an increased amount of pyridinic-N (Fig. 2g, Table S2). The localization of electrons near the Co center sites can be significantly reduced because of the high pyridinic-N, further heightening the collaboration with oxygen-containing species and thus optimizing the adsorption energy of intermediates (*O_2, *OOH, *OH, and *O) [41,42]. In addition, ZnCo-NGC has higher contents of graphitic-N than Zn-NC and Zn-NGC. By bonding to three carbon atoms, the graphitic-N with a lone electron can successfully weaken the O=O bond and favor oxygen reduction [43–45].

Fig. 2h illustrates that the Co 2p high-resolution spectrum for ZnCo-NC and ZnCo-NGC can be divided into three doublets, which consist of Co^{3+}, Co^{2+}, and Co^0. The fitting peaks at 780.7 and 796.3 eV correspond to the $2p_{3/2}$ and $2p_{1/2}$ orbits of Co^{3+}, respectively. The typical peaks at 782.1 and 797.5 eV are attributed to the $2p_{3/2}$ and $2p_{1/2}$ orbits for Co^{2+}. Furthermore, the peaks at 779.3 and 794.9 eV can be divided into the Co $2p_{3/2}$ and Co $2p_{1/2}$ states, which correspond to the metallic cobalt. The existence of intensive shake-up peaks at 785.5 and 804.2 eV also testifies the presence of Co(II) species in the samples. These results indicate that the oxidized and metallic states of cobalt are available for ZnCo-NC and ZnCo-NGC. ZnCo-NGC possesses a larger Co^0 peak area ratio than ZnCo-NC (Fig. 2i, Table S2). The abundance of metal particles in ZnCo-NGC can be attributed to the reduction of cobalt ions on imidazole carbides and graphene during high-temperature calcination. Some studies showed that Co nanoparticles inside graphitic carbon layers can modify the electronic structure of the metal-N_x active sites because of the electron-donating effect from the embedded nanoparticles and the nearby metal-N_x species. In addition, the metallic Co-inserted N-doped carbon provides a highly active site for ORR [46–49]. Moreover, the encapsulated metallic nanoparticles in CNTs could drive the fast reaction kinetics owing to the synergistic interaction between CNTs and Co nanoparticles. On the basis of these results, the high contents of pyridinic-N and graphitic-N for ZnCo-NGC help reduce the energy barrier of the intermediates and lower the charge-transfer resistance, further promoting ORR. The increased Co nanoparticles not only serve as active sites but also catalyze the continuous growth of CNTs, both of which improve the ORR catalytic activity.

Electrochemical performance

The ORR activity of the as-prepared samples was systematically explored through the three-electrode system. CV measurement was first conducted to measure the catalytic activity in the O_2-saturated 0.1 mol L^{-1} KOH solution (Fig. 3a). The typical redox peaks are found in the O_2-saturated electrolyte, whereas no peak

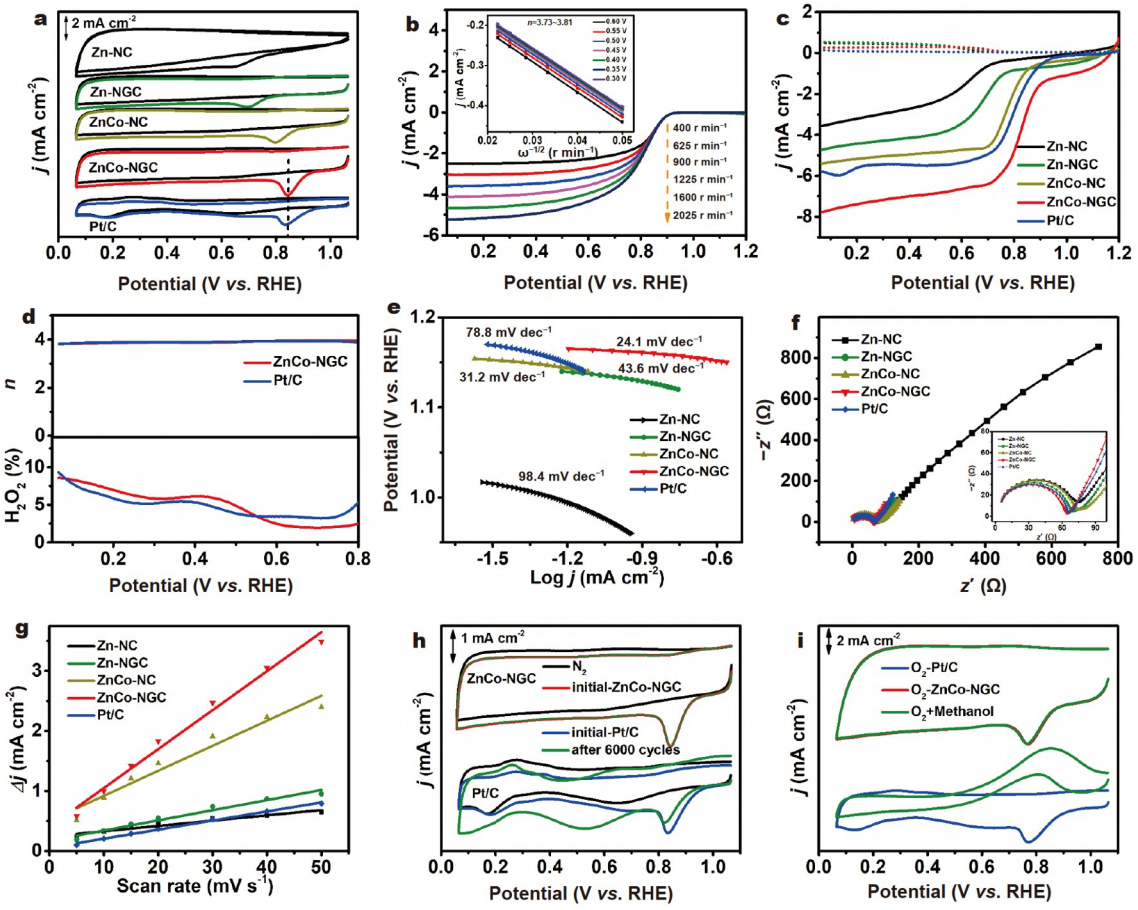

Figure 3 Electrocatalytic ORR performance in O_2-saturated 0.1 mol L^{-1} KOH electrolyte. (a) CV curves. (b) Linear sweep voltammetry (LSV) curves of ZnCo-NGC at different rotating speeds (inset: K-L plots at different potentials). (c) LSV curves with a rotation rate of 1600 r min^{-1}. (d) Electron transfer number (n) and H_2O_2 yield (H_2O_2%) of ZnCo-NGC and Pt/C. (e) Tafel slopes. (f) Nyquist plots and partial enlargement of Nyquist plots at the high frequency (inset). (g) Estimation of electrochemical double layer capacitance (C_{dl}). (h) Durability test for ZnCo-NGC and Pt/C. (i) Methanol tolerance test for ZnCo-NGC and Pt/C.

is observed in the N_2 atmosphere. The cathodic peaks of Zn-NC, Zn-NGC, ZnCo-NC, and ZnCo-NGC are located at 0.65, 0.70, 0.80, and 0.85 V, respectively. Among the samples, ZnCo-NGC shows the highest positive peak potential, outperforming the benchmark Pt/C (0.84 V), suggesting a prominent ORR activity. The ORR reaction pathway of ZnCo-NGC was further investigated by the rotating disk measurement at various rotation rates (400–2025 r min^{-1}). As shown in Fig. 3b, the resulting K-L equations for ZnCo-NGC at various potentials demonstrate nearly parallel relationships, indicating first-order reaction kinetics of the whole ORR process. The corresponding calculated electron transfer number at 0.30–0.60 V is calculated to be 3.73–3.81, thereby confirming the direct $4e^-$ pathway. RRDE tests were also performed to investigate the ORR activity of the obtained catalysts. As expected, ZnCo-NGC exhibits outstanding ORR performance ($E_{1/2}$ = 0.83 V, j_L = 7.74 mA cm^{-2}), which is superior to those of Zn-NC ($E_{1/2}$ = 0.59 V, j_L = 3.52 mA cm^{-2}), Zn-NGC ($E_{1/2}$ = 0.69 V, j_L = 4.74 mA cm^{-2}), ZnCo-NC ($E_{1/2}$ = 0.78 V, j_L = 5.38 mA cm^{-2}), and Pt/C ($E_{1/2}$ = 0.80 V, j_L = 5.80 mA cm^{-2}) (Fig. 3c). The transferred electron number and hydrogen peroxide yield of ZnCo-NGC are respectively determined to be 3.90% and 4.95% at the range of 0–0.80 V, which are close to those of the commercial Pt/C catalyst (n = 3.90, H_2O_2% = 4.86%) (Fig. 3d, Table S3). Thus, the ZnCo-NGC catalyst possesses an efficient four-electron pathway and preferable electrocatalytic selectivity. The high ORR activity of ZnCo-NGC is further reflected by the Tafel slope in Fig. 3e. ZnCo-NGC shows a smaller Tafel slope (24.1 mV dec^{-1}) than Zn-NC (98.4 mV dec^{-1}), Zn-NGC (43.6 mV dec^{-1}), ZnCo-NC (31.2 mV dec^{-1}), and Pt/C (78.8 mV dec^{-1}), revealing a fast reaction mechanism. Otherwise, the arc diameter on ZnCo-NGC over the high-medium frequency region is the smallest among all the samples, indicating that ZnCo-NGC has lower charge-transfer resistance compared with the other samples (Fig. 3f). The electrochemically active surface area measurements were evaluated based on the double layer capacitance (C_{dl}) to further investigate the ORR activity. ZnCo-NGC displays the largest C_{dl} value (64.9 mF cm^{-2}), indicating the existence of abundant active sites (Fig. 3g and Fig. S6).

The long-term stability of catalysts is another important performance parameter. In Fig. 3h, the continuous CV measurement of 6000 cycles in O_2-saturated KOH presents a negligible current loss and potential change for ZnCo-NGC, whereas the obviously negative shift of peak potential appears on the Pt/C electrode, indicating the better ORR catalytic stability of ZnCo-NGC than Pt/C. The excellent durability of ZnCo-NGC in the alkaline condition is correlative to the reason that the Co nanoparticles encapsulated in CNTs are physically isolated from the harsh environment, thus avoiding leaching. The corresponding cathodic ORR curves of ZnCo-NGC do not show a visible change when 3 mL of 3 mol L^{-1} methanol is introduced, whereas a reversed anodic peak occurs on the Pt/C electrode associated with methanol oxidation (Fig. 3i), suggesting the excellent methanol resistance of the ZnCo-NGC electrode. The above results demonstrate that the ZnCo-NGC catalyst exhibits superior ORR activity, durability, and methanol resistance in the alkaline electrolyte.

The ORR performance in O_2-saturated 0.5 mol L^{-1} H_2SO_4 solution was also investigated (Fig. 4). As illustrated in Fig. 4a, the cathodic peak is obviously detected at 0.73 V for ZnCo-NGC. LSV measurements were also conducted to depict the ORR activity of the obtained samples. All measurements were conducted at the rotating rate of 1600 r min^{-1} (scan rate ~10 mV s^{-1}), as shown in Fig. 4b. ZnCo-NGC represents the satisfactory catalytic activity for ORR with a half-wave potential of 0.73 V, closely approaching that of 20 wt% Pt/C ($E_{1/2}$ = 0.75 V). LSV measurements on RRDE were performed to explore the reaction pathway for ORR through identifying the content of intermediate H_2O_2. The transferred electron number and hydrogen peroxide yield of ZnCo-NGC are 3.85% and 7.28% from 0 to

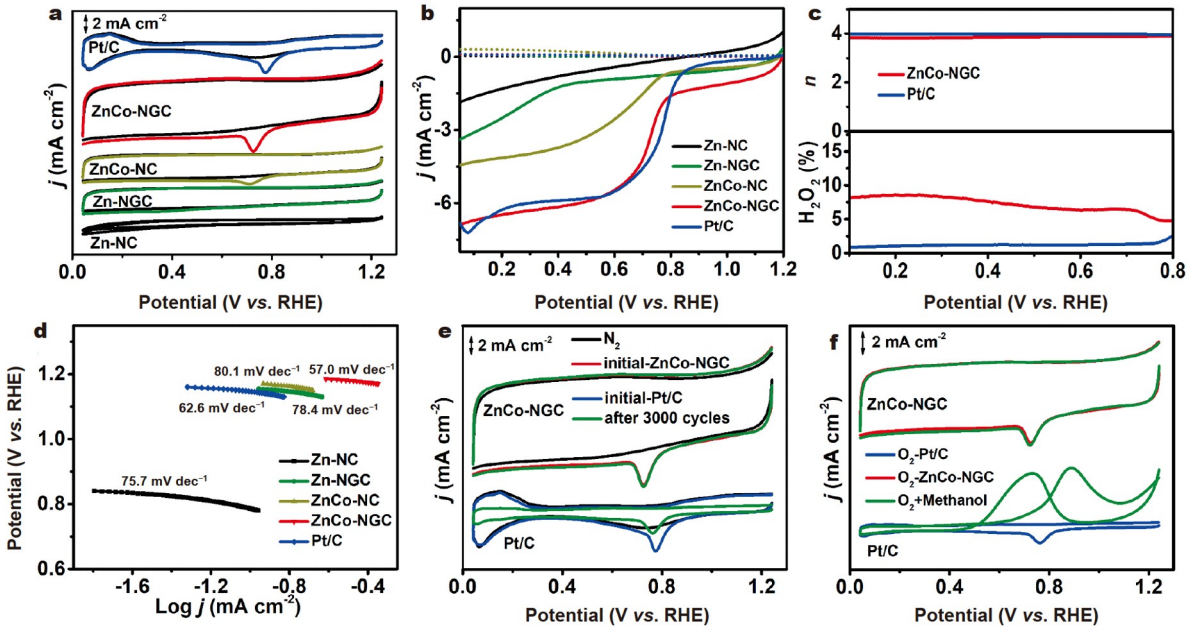

Figure 4 Electrocatalytic ORR performance in O_2-saturated 0.5 mol L^{-1} H_2SO_4 electrolyte. (a) CV curves. (b) LSV curves with a rotation rate of 1600 r min^{-1}. (c) Electron transfer number (n) and H_2O_2 yield (H_2O_2%) of ZnCo-NGC and Pt/C. (d) Tafel slopes. (e) The durability test for ZnCo-NGC and Pt/C. (f) The methanol tolerance test for ZnCo-NGC and Pt/C.

0.80 V, respectively, which are close to those of the Pt/C catalyst (n = 3.85, H_2O_2% = 7.67%), exhibiting a direct four-electron reaction pathway (Fig. 4c, Table S4). The smaller Tafel slope for ZnCo-NGC (57.0 mV dec^{-1}) than Pt/C (62.6 mV dec^{-1}) further verifies the superior activity (Fig. 4d). In addition, the ZnCo-NGC catalyst in acidic solution demonstrates impressive stability and methanol resistance (Fig. 4e, f). Therefore, the as-synthesized ZnCo-NGC sample can be utilized as an efficient ORR catalyst in acidic and alkaline conditions, revealing a promising application perspective.

The self-catalyzed growth of CNTs has a key effect on ORR performance. The key aspects for the self-catalyzed generation of CNTs contain two main points. One is the formation of metal nanoparticles, and the other is the diffusion of the carbon matrix. During pyrolysis, $Co(acac)_3$ within the cages is first reduced by the carbonization of organic linkers and precipitates on the surface of polyhedrons to produce Co nanoparticles. Simultaneously, the continuous diffusion of carbon atoms reaches around Co nanoparticles, and the self-catalyzed effect of Co nanoparticles benefits the *in situ* growth of CNTs. Thus, the formation of Co nanoparticles and carbon diffusion is an essential aspect for the self-catalyzed generation of CNTs.

GO nanosheets play an important role in oxygen reduction performance, which is reflected in the following aspects. (i) GO with oxygen functionalities can provide essential nucleation sites for the growth of metallic nanoparticles and prevent their agglomeration, which is crucial for the self-catalyzed growth of CNTs and enhancement of ORR performance. (ii) GO as an ideal 2D nanomaterial has particular electronic conductivity, enriching heterogeneous carbon supports and improving the electronic conductivity for ORR. (iii) GO containing abundant epoxy and hydroxyl functional groups can coordinate with the Zn ions in ZIF-8 and partially substitute 2-MEIM ligands together with maintaining the underlying coordination frameworks of ZIF-8, which can improve the structural stability of the ORR catalysts. (iv) The highly graphitized robust frameworks with rich pores are formed by the combination of ZIF-8 and moderate GO, promoting the transport of O_2 and electrolytes, thus enhancing the oxygen reduction activity.

In conclusion, the catalytic performances of ZnCo-NGC are superior to those of many reported catalysts (Tables S5 and S6). The remarkable electrocatalytic activity of ZnCo-NGC in alkaline and acidic solutions can be ascribed to the following advantages: (i) the special architecture of self-catalyzed grown N-CNTs can effectively reduce the aggregation of carbonaceous polyhedrons, leading to the abundantly exposed active sites and thus boosting electrochemical activity. (ii) The structure of hierarchical porous carbon with interconnected CNTs provides sufficient storage spaces and transport pathways for electrolyte ions during ORR. (iii) The appropriate nitrogen types and contents and the combination of reduced GO and *in situ* formed CNTs enhance the electron conductivity and generate accessible active sites in oxygen reduction. These virtues conjointly contribute to significantly boosting the electrochemical activity of the ZnCo-NGC catalyst for ORR.

Performance of ZABs

Considering the impressive ORR activity of the ZnCo-NGC catalyst, ZABs were established by using Zn foils as the anode, ZnCo-NGC catalysts as the cathode, and the 6 mol L^{-1} KOH solution mixed with 0.2 mol L^{-1} $Zn(OAc)_2$ as the electrolyte (Fig. 5a). As shown in Fig. 5b, the ZAB assembled with ZnCo-NGC displays a constant open-circuit voltage of 1.46 V, which is comparable to that of ZAB powered by Pt/C (1.51 V). The discharge polarization plots and the resultant power density plots are illustrated in Fig. 5c. The ZAB assembled with ZnCo-NGC suggests a higher peak power density (90 mW cm^{-2}) than ZAB with Pt/C (82 mW cm^{-2}). Fig. 5d demonstrates that the discharge voltages for ZAB driven by ZnCo-NGC are preferable to the one based on commercial Pt/C with an increasing current density. Obviously, the discharge voltage can be reestablished after decreasing the current density to the original low value, suggesting the impressive rate capabilities of ZnCo-NGC. Furthermore, the galvanostatic discharge-charge cycling curves are obtained with a constant current density of 1 mA cm^{-2} to evaluate the stability of the ZABs (Fig. 5e). The ZnCo-NGC-based

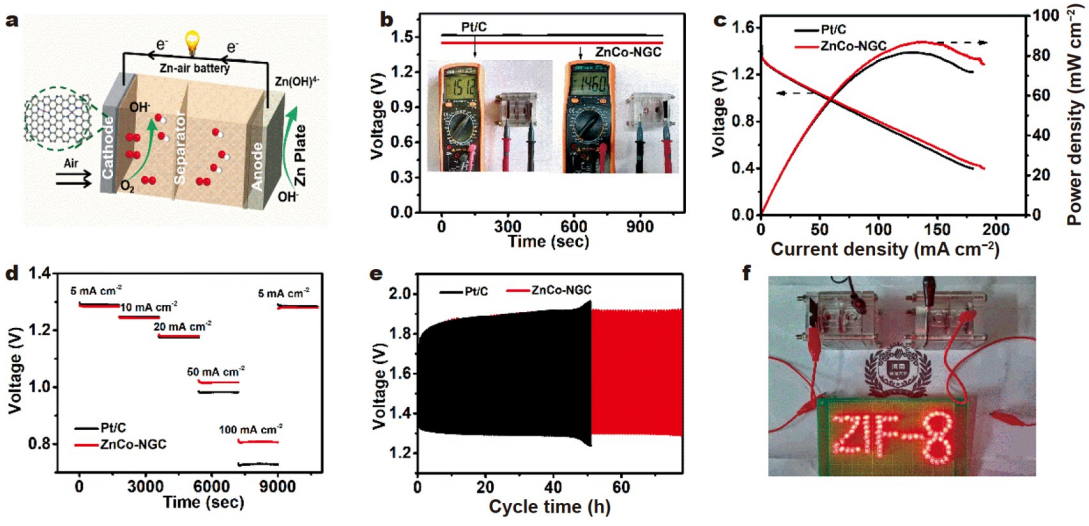

Figure 5 (a) Diagram of ZAB. (b) Open-circuit voltage plots of ZABs assembled with ZnCo-NGC and Pt/C catalysts (inset: photograph of the open-circuit potential). (c) Polarization and power curves of alkaline ZABs. (d) Galvanostatic discharge tests for the primary ZnCo-NGC-and Pt/C-based batteries with various current densities. (e) Discharge and charge cycling curves at 1 mA cm^{-2} of ZABs assembled with ZnCo-NGC and Pt/C. (f) Photograph of the lit red LEDs powered by two series of ZABs assembled by utilizing ZnCo-NGC catalysts.

ZAB exhibits exceptionally high cycle stability with negligible voltage decay of nearly 80 h. Two ZABs are connected in series to power a light-emitting diode (LED), confirming the promising application in energy storage (Fig. 5f). These results confirm that the established batteries have an excellent integration performance, enabling them to be competitive for practical applications.

CONCLUSION

We have developed an effective and facile ZIF-assisted strategy to construct the 3D carbonaceous polyhedrons linked by CNTs through pyrolyzing Co ions encapsulated in ZIF-8 intercalating GO sheets. The combination of reduced GO and *in situ* formed CNTs is conducive to improving the electronic conductivity of the catalysts. Moreover, the special N-CNT architecture can availably reduce the aggregation of carbonaceous polyhedrons, leading to additional exposed active sites and further boosting the electrochemical activity. Given these features, the optimized ZnCo-NGC exhibits impressive ORR performance in 0.1 mol L^{-1} KOH solution ($E_{1/2}$ = 0.83 V) and 0.5 mol L^{-1} H_2SO_4 electrolyte ($E_{1/2}$ = 0.73 V), which are very close to those of the commercial Pt/C catalyst ($E_{1/2}$ = 0.80 V in 0.1 mol L^{-1} KOH, $E_{1/2}$ = 0.75 V in 0.5 mol L^{-1} H_2SO_4). In addition, satisfactory cycling stability and methanol resistance are achieved in alkaline and acidic solutions, making ZnCo-NGC become a competitive Pt-free alternative for ORR. Moreover, the ZAB assembled with ZnCo-NGC can present comparable power density and excellent charge/discharge cycle stability to batteries driven by commercial Pt/C catalysts. This work not only provides promising guidance for designing high-performance ORR catalysts with *in situ* formed CNTs but also demonstrates practical applications in electrochemical energy storage and conversion.

Received 16 June 2021; accepted 16 August 2021; published online 24 September 2021

1 Aricò AS, Bruce P, Scrosati B, *et al.* Nanostructured materials for advanced energy conversion and storage devices. Nat Mater, 2005, 4: 366–377
2 Liu Q, Wang Y, Dai L, *et al.* Scalable fabrication of nanoporous carbon fiber films as bifunctional catalytic electrodes for flexible Zn-air batteries. Adv Mater, 2016, 28: 3000–3006
3 Rao H, Schmidt LC, Bonin J, *et al.* Visible-light-driven methane formation from CO_2 with a molecular iron catalyst. Nature, 2017, 548: 74–77
4 Tarascon JM, Armand M. Issues and challenges facing rechargeable lithium batteries. Nature, 2001, 414: 359–367
5 Winter M, Brodd RJ. What are batteries, fuel cells, and supercapacitors? Chem Rev, 2004, 104: 4245–4270
6 Liu X, Yuan Y, Liu J, *et al.* Utilizing solar energy to improve the oxygen evolution reaction kinetics in zinc-air battery. Nat Commun, 2019, 10: 4767
7 Du L, Prabhakaran V, Xie X, *et al.* Low-PGM and PGM-free catalysts for proton exchange membrane fuel cells: Stability challenges and material solutions. Adv Mater, 2021, 33: 1908232
8 Wang Y, Song Y, Xia Y. Electrochemical capacitors: Mechanism, materials, systems, characterization and applications. Chem Soc Rev, 2016, 45: 5925–5950
9 Nie Y, Li L, Wei Z. Recent advancements in Pt and Pt-free catalysts for oxygen reduction reaction. Chem Soc Rev, 2015, 44: 2168–2201
10 Galiote NA, Oliveira FER, Lima FHB. FeCo-N-C oxygen reduction electrocatalysts: Activity of the different compounds produced during the synthesis *via* pyrolysis. Appl Catal B-Environ, 2019, 253: 300–308
11 He Y, Guo H, Hwang S, *et al.* Single cobalt sites dispersed in hierarchically porous nanofiber networks for durable and high-power PGM-free cathodes in fuel cells. Adv Mater, 2020, 32: 2003577
12 Wang HF, Chen L, Pang H, *et al.* MOF-derived electrocatalysts for oxygen reduction, oxygen evolution and hydrogen evolution reactions. Chem Soc Rev, 2020, 49: 1414–1448
13 Sun JK, Xu Q. Functional materials derived from open framework templates/precursors: Synthesis and applications. Energy Environ Sci, 2014, 7: 2071–2100
14 Xia W, Mahmood A, Zou R, *et al.* Metal-organic frameworks and their derived nanostructures for electrochemical energy storage and conversion. Energy Environ Sci, 2015, 8: 1837–1866
15 Qu G, Zhang X, Xiang G, *et al.* ZIF-67 derived hollow Ni-Co-Se nanopolyhedrons for flexible hybrid supercapacitors with remarkable electrochemical performances. Chin Chem Lett, 2020, 31: 2007–2012
16 Xiang G, Meng Y, Qu G, *et al.* Dual-functional $NiCo_2S_4$ polyhedral architecture with superior electrochemical performance for supercapacitors and lithium-ion batteries. Sci Bull, 2020, 65: 443–451
17 Cheng N, Ren L, Xu X, *et al.* Recent development of zeolitic imidazolate frameworks (ZIFs) derived porous carbon based materials as electrocatalysts. Adv Energy Mater, 2018, 8: 1801257
18 Zhang L, Su Z, Jiang F, *et al.* Highly graphitized nitrogen-doped porous carbon nanopolyhedra derived from ZIF-8 nanocrystals as efficient electrocatalysts for oxygen reduction reactions. Nanoscale, 2014, 6: 6590–6602
19 Zhong S, Zhan C, Cao D. Zeolitic imidazolate framework-derived nitrogen-doped porous carbons as high performance supercapacitor electrode materials. Carbon, 2015, 85: 51–59
20 Wang T, Wang J, Wang X, *et al.* Graphene-templated synthesis of sandwich-like porous carbon nanosheets for efficient oxygen reduction reaction in both alkaline and acidic media. Sci China Mater, 2018, 61: 915–925
21 Li L, He J, Wang Y, *et al.* Metal-organic frameworks: A promising platform for constructing non-noble electrocatalysts for the oxygen-reduction reaction. J Mater Chem A, 2019, 7: 1964–1988
22 Ahn SH, Yu X, Manthiram A. "Wiring" Fe-N_x-embedded porous carbon framework onto 1D nanotubes for efficient oxygen reduction reaction in alkaline and acidic media. Adv Mater, 2017, 29: 1606534
23 Yan D, Guo L, Xie C, *et al.* N, P-dual doped carbon with trace Co and rich edge sites as highly efficient electrocatalyst for oxygen reduction reaction. Sci China Mater, 2018, 61: 679–685
24 Wu S, Zhu Y, Huo Y, *et al.* Bimetallic organic frameworks derived CuNi/carbon nanocomposites as efficient electrocatalysts for oxygen reduction reaction. Sci China Mater, 2017, 60: 654–663
25 Lu W, Shen J, Zhang P, *et al.* Construction of CoO/Co-Cu-S hierarchical tubular heterostructures for hybrid supercapacitors. Angew Chem Int Ed, 2019, 58: 15441–15447
26 Lu Q, Yu J, Zou X, *et al.* Self-catalyzed growth of Co, N-codoped CNTs on carbon-encased CoS_x surface: A noble-metal-free bifunctional oxygen electrocatalyst for flexible solid Zn-air batteries. Adv Funct Mater, 2019, 29: 1904481
27 Yang F, Liu X, Zhang H, *et al.* Boosting oxygen catalytic kinetics of carbon nanotubes by oxygen-induced electron density modulation for advanced Zn-air batteries. Energy Storage Mater, 2020, 30: 138–145
28 Tang C, Wang B, Wang HF, *et al.* Defect engineering toward atomic Co-N_x-C in hierarchical graphene for rechargeable flexible solid Zn-air batteries. Adv Mater, 2017, 29: 1703185
29 Yan L, Xu Y, Chen P, *et al.* A freestanding 3D heterostructure film stitched by MOF-derived carbon nanotube microsphere superstructure and reduced graphene oxide sheets: A superior multifunctional electrode for overall water splitting and Zn-air batteries. Adv Mater, 2020, 32: 2003313
30 Meng J, Niu C, Xu L, *et al.* General oriented formation of carbon nanotubes from metal-organic frameworks. J Am Chem Soc, 2017, 139: 8212–8221
31 Wang J, Liu W, Luo G, *et al.* Synergistic effect of well-defined dual sites boosting the oxygen reduction reaction. Energy Environ Sci, 2018, 11: 3375–3379
32 Choi CH, Chung MW, Kwon HC, *et al.* Nitrogen-doped graphene/carbon nanotube self-assembly for efficient oxygen reduction reaction in acid media. Appl Catal B-Environ, 2014, 144: 760–766

33 Zhang G, Jin X, Li H, *et al.* N-doped crumpled graphene: Bottom-up synthesis and its superior oxygen reduction performance. Sci China Mater, 2016, 59: 337–347
34 Shao Q, Liu J, Wu Q, *et al. In situ* coupling strategy for anchoring monodisperse Co_9S_8 nanoparticles on S and N dual-doped graphene as a bifunctional electrocatalyst for rechargeable Zn-air battery. Nano-Micro Lett, 2019, 11: 4
35 Li Y, Cui M, Li T, *et al.* Embedding Co_2P nanoparticles into co-doped carbon hollow polyhedron as a bifunctional electrocatalyst for efficient overall water splitting. Int J Hydrogen Energy, 2020, 45: 16540–16549
36 Chang X, Ma Y, Yang M, *et al. In-situ* solid-state growth of N, S codoped carbon nanotubes encapsulating metal sulfides for high-efficient-stable sodium ion storage. Energy Storage Mater, 2019, 23: 358–366
37 Li X, Guan BY, Gao S, *et al.* A general dual-templating approach to biomass-derived hierarchically porous heteroatom-doped carbon materials for enhanced electrocatalytic oxygen reduction. Energy Environ Sci, 2019, 12: 648–655
38 Wang Y, Alsmeyer DC, McCreery RL. Raman spectroscopy of carbon materials: Structural basis of observed spectra. Chem Mater, 1990, 2: 557–563
39 Tan B, Wu ZF, Xie ZL. Fine decoration of carbon nanotubes with metal organic frameworks for enhanced performance in supercapacitance and oxygen reduction reaction. Sci Bull, 2017, 62: 1132–1141
40 Shao Q, Li Y, Cui X, *et al.* Metallophthalocyanine-based polymer-derived Co_2P nanoparticles anchoring on doped graphene as high-efficient trifunctional electrocatalyst for Zn-air batteries and water splitting. ACS Sustain Chem Eng, 2020, 8: 6422–6432
41 Kulkarni A, Siahrostami S, Patel A, *et al.* Understanding catalytic activity trends in the oxygen reduction reaction. Chem Rev, 2018, 118: 2302–2312
42 Wang W, Jia Q, Mukerjee S, *et al.* Recent insights into the oxygen-reduction electrocatalysis of Fe/N/C materials. ACS Catal, 2019, 9: 10126–10141
43 Wang Y, Zhu C, Feng S, *et al.* Interconnected Fe, S, N-codoped hollow and porous carbon nanorods as efficient electrocatalysts for the oxygen reduction reaction. ACS Appl Mater Interfaces, 2017, 9: 40298–40306
44 Li Q, Chen W, Xiao H, *et al.* Fe isolated single atoms on S, N codoped carbon by copolymer pyrolysis strategy for highly efficient oxygen reduction reaction. Adv Mater, 2018, 30: 1800588
45 Shang C, Yang M, Wang Z, *et al.* Encapsulated MnO in N-doping carbon nanofibers as efficient ORR electrocatalysts. Sci China Mater, 2017, 60: 937–946
46 Zhang X, Lin J, Chen S, *et al.* Co nanoparticles encapsulated in N-doped carbon nanosheets: Enhancing oxygen reduction catalysis without metal-nitrogen bonding. ACS Appl Mater Interfaces, 2017, 9: 38499–38506
47 Sun X, Tang D, Zhang W, *et al.* Molten salt synthesis of Co-entrapped, N-doped porous carbon from various nitrogen precursors as efficient electrocatalysts for hydrogen evolution. J Mater Sci, 2019, 54: 638–647
48 Aijaz A, Masa J, Rösler C, *et al.* Co@Co_3O_4 encapsulated in carbon nanotube-grafted nitrogen-doped carbon polyhedra as an advanced bifunctional oxygen electrode. Angew Chem Int Ed, 2016, 55: 4087–4091
49 Guan C, Sumboja A, Wu H, *et al.* Hollow Co_3O_4 nanosphere embedded in carbon arrays for stable and flexible solid-state zinc-air batteries. Adv Mater, 2017, 29: 1704117

Acknowledgements This work was supported by the National Natural Science Foundation of China (51872076 and U1804255), the Program for Innovative Research Team of Henan Scientific Committee (CXTD2014033), the Project of Central Plains Science and Technology Innovation Leading Talents of Henan Province (194200510001) and the Scientific and Technological Research Project of Henan province (212102210651).

Author contributions Gao S, Liu X and Zhang J conceived and designed the experiments. Zhang J, Chen Y and Liu Y performed the experiments and characterizations. Gao S, Liu X and Zhang J wrote the paper. All authors participated in the general discussion.

Conflict of interest The authors declare that they have no conflict of interest.

Supplementary information Supporting data are available in the online version of the paper.

Jing Zhang is a postgraduate student in Prof. Shuyan Gao's group at Henan Normal University. Her current research interest includes carbon-based electrocatalysts and their application in Zn-air battery.

Xupo Liu received his PhD degree from China University of Geosciences (Wuhan) in 2018. He worked as a postdoctoral researcher under the supervision of Prof. Deli Wang at Huazhong University of Science and Technology from July 2018 to July 2020. He is currently a lecturer at Henan Normal University. His research interests focus on carbon materials, non-noble metal electrocatalysts, self-supporting electrodes, and their applications for fuel cells and water splitting.

Shuyan Gao received her PhD degree from Changchun Institute of Applied Chemistry, Chinese Academy of Sciences in 2006. She worked as a Japan Science Promotion Society research fellow at the National Institute of Advanced Industrial Science and Technology (2007–2009). Afterward, she was a specially appointed professor at Hokkaido University. She is currently a professor at Henan Normal University. Her research includes the utilization of environmental waste resources to build energy storage and conversion materials, additive manufacturing of triboelectric nanogenerators, and their applications in self-power electrocatalysis field.

MOFs衍生自催化生长Zn/Co-N-C碳纳米管用作锌空气电池高效氧还原催化剂

张静, 陈野, 刘洋, 刘旭坡*, 高书燕*

摘要 开发高性价比、高性能碳基氧还原反应(ORR)电催化剂对于锌空气电池发展至关重要. 本工作通过一锅合成法构建自催化生长碳纳米管(CNTs)交联的Zn/Co-N-C碳质多面体, 该碳纳米管由氧化石墨烯纳米片连接的沸石咪唑框架(ZIF-8)衍生而来. 该特殊氮掺杂三维碳基体可以调控活性中心暴露以及金属纳米粒子和碳纳米管的协同作用. 该催化剂在0.1 mol L^{-1} KOH ($E_{1/2}$ = 0.83 V)和0.5 mol L^{-1} H_2SO_4 ($E_{1/2}$ = 0.73 V)中均表现出优良的ORR活性、循环稳定性和耐甲醇性, 性能与Pt/C相当(0.1 mol L^{-1} KOH, $E_{1/2}$=0.80 V; 0.5 mol L^{-1} H_2SO_4, $E_{1/2}$ = 0.75 V). 由该催化剂组装的锌空气电池表现出高功率密度(90 mW cm^{-2})和优异的循环稳定性, 优于Pt/C (82 mW cm^{-2}). 本工作为原位合成高效碳纳米管ORR催化剂提供了有力指导, 并为便携式锌空气电池器件研究提供了良好借鉴.

